Scientific Visualization, 2026, volume 18, number 3, pages 41 - 51, DOI: 10.26583/sv.18.3.04

# Deep-Learning-Based Workflow for Cavern Segmentation and Derived Profile Construction from Core Photos

D.O. Makienko[1,A,B], G.A. Kossov[2,A], V.V. Abashkin[3,A], I.A. Seleznev[4,A], I.V. Safonov[5,A,B]

[A] LLC STISS, Moscow, Russia
[B] National Research Nuclear University "MEPhI", Moscow, Russia

[1] ORCID: 0000-0001-7341-6128, dmakienko@slb.ru
[2] ORCID: 0009-0001-7012-6069, gkossov@slb.ru
[3] ORCID: 0009-0003-9827-1780, vabashkin@slb.ru
[4] ORCID: 0009-0007-7977-4904, iseleznev@slb.ru
[5] ORCID: 0000-0002-8270-943X, isafonov@slb.ru

**Abstract**

To estimate hydrocarbon reserves and plan production, geologists construct reservoir models that describe lithofacies variations with depth. In carbonate rocks, caverns provide important information about storage capacity and fluid flow potential. Photographs of core samples allow analysis of surface-visible caverns. Segmentation of cavern-like objects in core photographs enables profile construction to identify depth intervals where lithofacies change, reflecting variations in sedimentation conditions and corresponding reservoir properties. Rock heterogeneity, varying imaging conditions, and non-target structures such as fractures and artifacts complicate cavern analysis from photographs. This paper proposes a deep-learning-based workflow for segmentation of cavern-like objects for visualization of the cavernosity profile intended to support lithofacies delineation. The workflow includes semi-automatic annotation preparation for training a deep learning segmentation model. Model training relies on augmented images to account for varying brightness distributions. The segmentation results enable visualization of the depth-dependent profile that qualitatively reflects the distribution of cavern-like objects and may support description and delineation of lithofacies.

**Keywords**: cavern segmentation, cavernosity visualization, lithofacies delineation.

## Introduction

The oil and gas industry uses geological reservoir models to estimate reserves and plan production. Building geological reservoir models requires depth-based lithofacies delineation in wells, reflecting variations in sedimentation conditions and corresponding reservoir properties. In carbonate reservoirs, cavernosity is an important characteristic for lithofacies delineation. Cavernous layers contain large and spatially heterogeneous voids known as caverns. Cavernous layers require detailed analysis because they may contain significant hydrocarbon volumes; however, the feasibility of production depends on the connectivity of caverns with fractures and pores, as well as on the number, volume, and shape of the caverns [1, 2].

Various techniques support analysis of caverns. Caverns appear as low-density objects in computed tomography data of core samples [1, 3], as dark voids in optical photographs of core samples or optical borehole wall images [4], and as objects of increased electrical conductivity or acoustic scattering in borehole wall images [2, 5, 6]. These techniques differ in their analysis domains, as computed tomography reflects the internal structure of extracted core samples, photographs typically show the lateral surface of core samples from a particular viewpoint, and borehole images display measured characteristics on the borehole wall sur-

face. In addition, the techniques differ in the ambiguities associated with interpreting objects as caverns. None of the techniques provides a precise estimate of cavernosity, and technique comparison therefore relies primarily on qualitative analysis.

During field development, operators extract core samples from multiple wells across broad depth intervals. Core-handling procedures typically include photography, making core photographs one of the earliest and most accessible sources of information for lithofacies delineation. Photographs provide the basis for analysis of color and texture characteristics of cores [7, 8, 9, 10, 11, 12]. In particular, core photographs enable analysis of surface-visible caverns (Figure 1) and can support construction of a depth-dependent profile that qualitatively reflects variations in cavernosity. However, reliable cavern identification remains challenging, even for experts. For example, some fractures and rock chips may resemble caverns. Therefore, in the context of core photographs, it is more appropriate to refer to the detection of cavern-like objects rather than true caverns (in the geological sense) only.



Figure 1. Cavernous core samples. The height of the two samples on the left is 15 cm. The height of the six samples on the right is 5 cm.

Rock heterogeneity, non-uniform illumination during image acquisition, and the presence of non-target dark objects increase the complexity and ambiguity of cavern detection from photographs. This study proposes a deep-learning-based workflow to segment cavern-like objects and construct a derived profile intended to support lithofacies delineation. The workflow includes semi-automatic annotation with subsequent manual refinement, model training on augmented images for cavern segmentation, model inference on core photographs ordered by well depth, construction and visualization of the cavernosity profile.

## Materials and Methods

The proposed workflow for cavern segmentation and cavernosity profile construction from core photographs consists of three stages (Figure 2). The first stage involves preparation of cavernous rock photos and cavern annotation. The second stage splits the photographs into training and test sets, extracts patches from core photos, and trains a deep neural network on augmented data. The third stage extracts patches from the depth-ordered photographs, applies the segmentation model to the extracted patches, aggregates the segmentation results according to their positions in the original photographs, and constructs and visualizes the cavernosity profile.

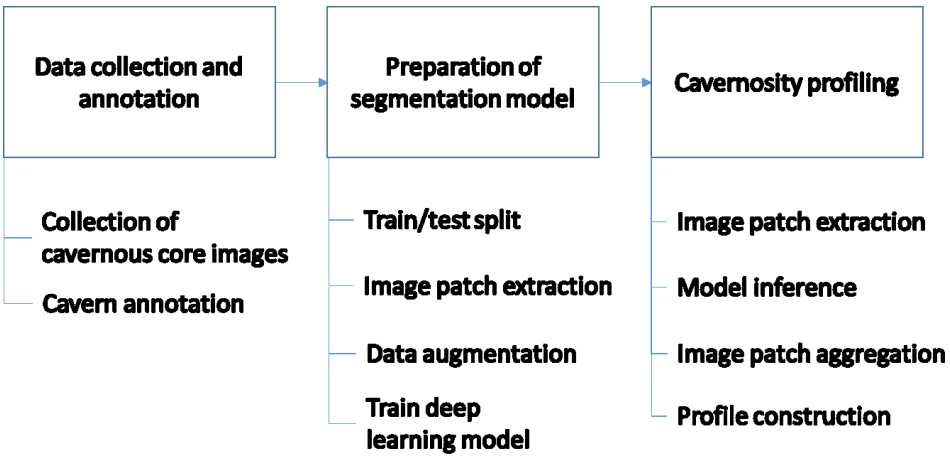


Figure 2. The workflow scheme

# Data collection and annotation

State and corporate standards guide the preparation of core samples extracted from wells for storage and analysis [13, 14]. Drilling produces cylindrical core samples. In practice, operators often slab the cores along a plane parallel to the cylinder's vertical axis to expose an internal cross-section unaffected by drilling. Trays then organize cylindrical or slabbed samples according to well. Both slabbed and cylindrical core samples are suitable for cavernosity analysis.

During image acquisition, the setup positions core samples horizontally. The camera mounts overhead with its optical axis perpendicular to the sample plane. Core photographs show the lateral surface of the samples from a single viewpoint. Core trays typically contain a depth scale bar and a color calibration target. Although standards do not define quantitative lighting requirements, illumination should preserve the natural color and texture of the samples. In practice, lighting setups vary in consistency and quality [15]. Color correction methods based on calibration targets exist [16], but they require uniform lighting, which is not always achievable.

Cavern annotation follows a semi-automatic workflow. Image grouping follows rock type, imaging conditions, and the degree of rock destruction. Each image group uses its own processing parameters. Processing includes binarization and object selection based on shape and brightness characteristics. A geologist performed minor annotation refinement, including removal of falsely detected objects (such as dark mineral inclusions, fractures, and markings) and addition of missed objects. Two additional geologists reviewed the resulting annotations to identify potential inconsistencies.

The binarization step applies adaptive thresholding as implemented in the OpenCV library [17]. An adaptive threshold is determined individually for different image regions. An adaptive threshold may be preferable to a global threshold due to varying brightness distributions of core images. The binarization threshold is the weighted average of the intensity values within a sliding window that moves across the image:

$$T_{xy} = \sum_{i=0}^{n-1} \sum_{j=0}^{n-1} w(i,j) I(i+x, j+y) - c^*, \quad (1)$$

$$wg(i,j) = e^{-\frac{(i-\mu)^2+(j-\mu)^2}{2\sigma^2}}, \quad (2)$$

$$\mu = \frac{n-1}{2}, \sigma = 0.3\left(\frac{n-1}{2} - 1\right) + 0.8, \quad (3)$$

$$w(i,j) = \frac{wg(i,j)}{\sum_{i=0}^{n-1} \sum_{j=0}^{n-1} wg(i,j)}, \quad (4)$$

$$c^* = \arg\max_{c \in C} N(c), \quad (5)$$

where $I$ is the image, $n$ is the window size, $w$ is the Gaussian-distributed weights with mean $\mu$ and variance $\sigma^2$, $(x, y)$ is the current position of the window. The value $c^* \in C$ corresponds to the binarization result that produces the highest number of segments $N$.

The method selects segments from connected components based on area, aspect ratio, and brightness. Thresholds on minimum and maximum area, maximum brightness, and maximum aspect ratio define the selection criteria. The following formulas calculate the area and aspect ratio of the segment:

$$Area = \sum_{x=1}^{M} \sum_{y=1}^{N} p(x, y), \tag{6}$$

$$Aspect\ Ratio = \frac{\max(L, W)}{\min(L, W)}, \tag{7}$$

$$L = 2\sqrt{\frac{2\left(\mu_{20} + \mu_{02} + \sqrt{(\mu_{20} - \mu_{02})^2 + 4\mu_{11}^2}\right)}{\mu_{00}}}, \tag{8}$$

$$W = 2\sqrt{\frac{2\left(\mu_{20} + \mu_{02} - \sqrt{(\mu_{20} - \mu_{02})^2 + 4\mu_{11}^2}\right)}{\mu_{00}}}, \tag{9}$$

$$\mu_{pq} = \sum_{x=1}^{M} \sum_{y=1}^{N} (x - x_c)^p (y - y_c)^q p(x, y), \tag{10}$$

$$x_c = \frac{\sum_{x=1}^{M} \sum_{y=1}^{N} x\, p(x, y)}{\sum_{x=1}^{M} \sum_{y=1}^{N} p(x, y)}, \qquad y_c = \frac{\sum_{x=1}^{M} \sum_{y=1}^{N} y\, p(x, y)}{\sum_{x=1}^{M} \sum_{y=1}^{N} p(x, y)}, \tag{11}$$

where $M$, $N$ are the width and height of the image, $p(x, y) = 1$ for segment and $p(x, y) = 0$ otherwise, $L, W$ are the length and width of the segment.

## Model training

The dataset comprises 50 photographs of core samples covering 40 m of core. The photographs represent a wide range of cavernosity appearances and include core samples from Russian fields and the Kansas Geological Survey [18]. Splitting the data into training, validation, and test sets precedes patch extraction. The split does not consider the data source (Russian fields or the Kansas Geological Survey). Instead, photographs of directly adjacent depth intervals with similar rock appearance and imaging conditions remain within the same subset to prevent data leakage. The training, validation, and test sets contain 36, 7, and 7 photographs, respectively. Patch extraction produces image patches of 512 × 512 pixels, corresponding to a physical area of 5.12 × 5.12 cm². The training set contains 1,500 patches, whereas the validation and test sets each contain 300 patches. Patches extracted from core photographs serve as input to the deep learning model.

The training pipeline applies data augmentation to improve the network's generalization capability. The augmentation includes image rotation, brightness distribution adjustment, blurring and noise injection [19]. The augmentation procedure randomly selects distortion parameters. To vary brightness distribution, it applies gamma correction with a gamma value sampled from the range [0.3, 3.0]. To simulate blur, it convolves the image with a Gaussian kernel having a standard deviation sampled from the range [0.8, 2.6] pixels. The procedure also adds Gaussian noise, with noise values sampled from a normal distribution with a mean of 0 and a standard deviation of 0.15 for image intensities normalized to the range [0, 1].

For cavern segmentation, this study employs the U-Net architecture with a ResNet-18 backbone pre-trained on the ImageNet dataset [20, 21]. This approach combines the robust feature extraction capabilities of deep residual networks with the precise localization mechanism of U-Net's skip connections. By integrating low-level details from the encoder with high-level information in the decoder, the model effectively restores spatial relationships.

Table 1 summarizes the model parameters. The Weighted Cross-Entropy loss function addresses the significant class imbalance between 'cavern' and 'background' pixels. To compensate for class imbalance, the error weight for cavern class exceeds the error weight for the background class. The Adam optimizer updates model weights [22]. The parameters follow the original method recommendations. The initial learning rate is set to 0.001. The $\beta_1$ and $\beta_2$ parameters, which control the moving averages of the gradient and its square, are set to 0.9 and 0.999, respectively. The training procedure uses a batch size of 96 and allows up to 50 training epochs. Early stopping terminates training when the validation loss does not improve for five consecutive epochs. During inference, a probability threshold of 0.5 generates the binary segmentation result.

Table 1. Deep-learning model parameters

| | |
|---|---|
| architecture | U-Net |
| backbone | Resnet-18 |
| loss | Weighted Cross-Entropy |
| optimizer | Adam |
| learning rate | 0.001 |
| maximum number of epochs | 50 |
| early stopping patience | 5 epochs |
| batch size | 96 |
| binarization threshold | 0.5 |

## Cavernosity profiling

For cavern segmentation on test images, the method employs image patch extraction with overlap. The trained model estimates the probability of each pixel belonging to the cavern class. The aggregation step combines the probability maps onto the image by averaging values in overlapping regions. Finally, applying a threshold to the probability map generates the binary segmentation result.

The method constructs and visualizes the cavernosity profile. The profile represents the fraction of pixels classified as cavern-like within a sliding window that moves along depth with overlap. The sliding window size and step depend on the analysis requirements. At the boundaries of the processing interval (top/bottom) and in gap zones with missing images, the approach adaptively reduces the averaging area, using up to 50% of the window size at boundary points.

## Results and Discussion

This study assesses the segmentation model on the original and the distorted images from the test set. The evaluation uses gamma correction to simulate variations in brightness distribution because obtaining a representative dataset of photographs acquired under different imaging conditions is challenging. For the first distortion group, gamma-correction coefficients randomly sampled from the range [1.1, 3.0] reduced overall image brightness and decreased contrast in dark regions. For the second distortion group, coefficients randomly sampled from the range [0.3, 0.9] increased overall image brightness and enhanced contrast in dark regions.

The study quantified segmentation quality using the IoU, Dice, Precision, and Recall metrics by comparing the segmentation results with the annotations obtained using the procedure described in the “Data Collection and Annotation” section. The IoU metric measures the ratio of the intersection between cavern-like objects in the annotations and the segmentation results to their union. Recall quantifies the proportion of annotated cavern-like pixels correctly identified by the model. Precision measures the proportion of pixels predicted as cavern-like that are also present in the annotations. The Dice coefficient represents the harmonic mean of Precision and Recall. Table 2 presents the metric values.

Table 2. Segmentation quality metrics for the test dataset

| Quality metric | Original | Distortion 1 | Distortion 2 |
|---|---|---|---|
| Dice | 0.77 | 0.78 | 0.78 |
| IoU | 0.62 | 0.64 | 0.64 |
| Precision | 0.71 | 0.72 | 0.76 |
| Recall | 0.84 | 0.87 | 0.80 |

The reported metrics demonstrate that the model generalizes well to photographs with varying brightness distributions. The Dice and IoU scores differ by no more than 0.03 across the evaluated distortion conditions. Precision ranges from 0.71 to 0.76, whereas Recall ranges from 0.80 to 0.87. Figure 3 shows the images with varying brightness distributions alongside visualization maps that highlight agreements and discrepancies between the model predictions and the annotations. Green regions indicate the overlap between the predictions and the annotations. Blue regions correspond to annotated areas missed by the model, whereas orange regions indicate areas predicted by the model but absent from the annotations.

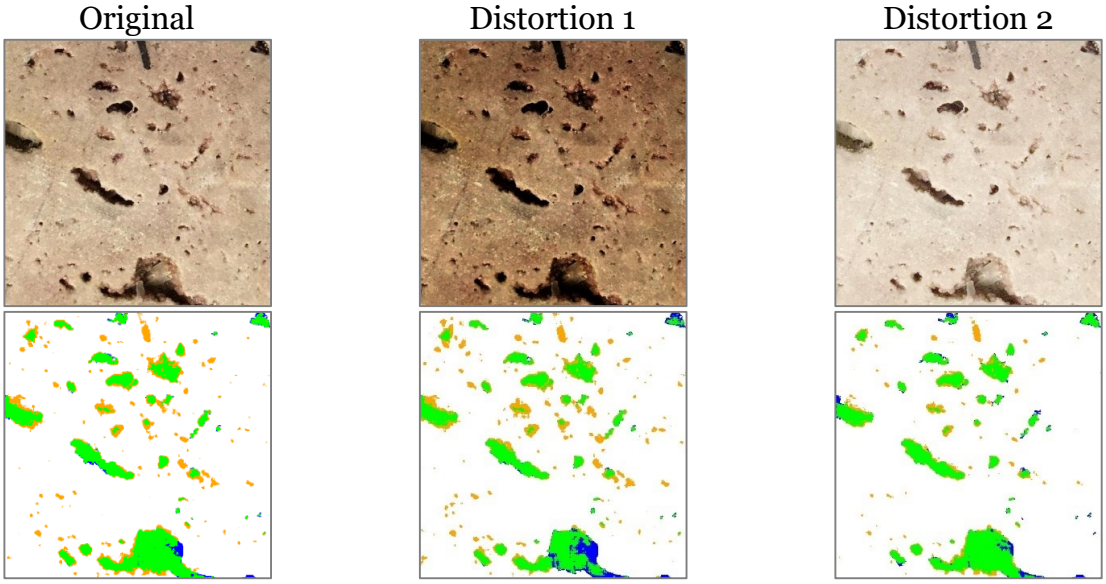



Figure 3. Segmentation results for the original and gamma-corrected images

Discrepancies between the model predictions and the annotations primarily occur near object boundaries and for visually ambiguous structures (Figure 4). The model occasionally misclassifies parts of fractures or other dark objects as caverns. False positives also occur for dark markings present on the core samples. The large variability in marking styles makes it difficult to represent all possible markings in the training dataset and, consequently, to train a model that reliably distinguishes them from large caverns. Therefore, when core sample preparation procedures include handwritten markings, their automatic detection and inpainting prior to cavern segmentation may improve the resulting segmentation quality [23].

Figures 5 and 6 illustrate cavern segmentation results and the derived profiles for core samples. The height of the samples is 30 cm. The figures show both the original and distorted images. Visualization maps displayed next to the photographs highlight agreements and discrepancies between the model predictions and the annotations. The right side of each figure presents cavernosity profiles constructed from the segmentation results. The sliding window used to construct the profiles has a height of 5 mm and moves with a 1 mm step. The horizontal scale of the profiles reflects the proportion of pixels in the sliding window predicted as caverns. The black profile corresponds to the original photo, the blue profile corresponds to the first type of distortion, and the red profile corresponds to the second type of distortion.

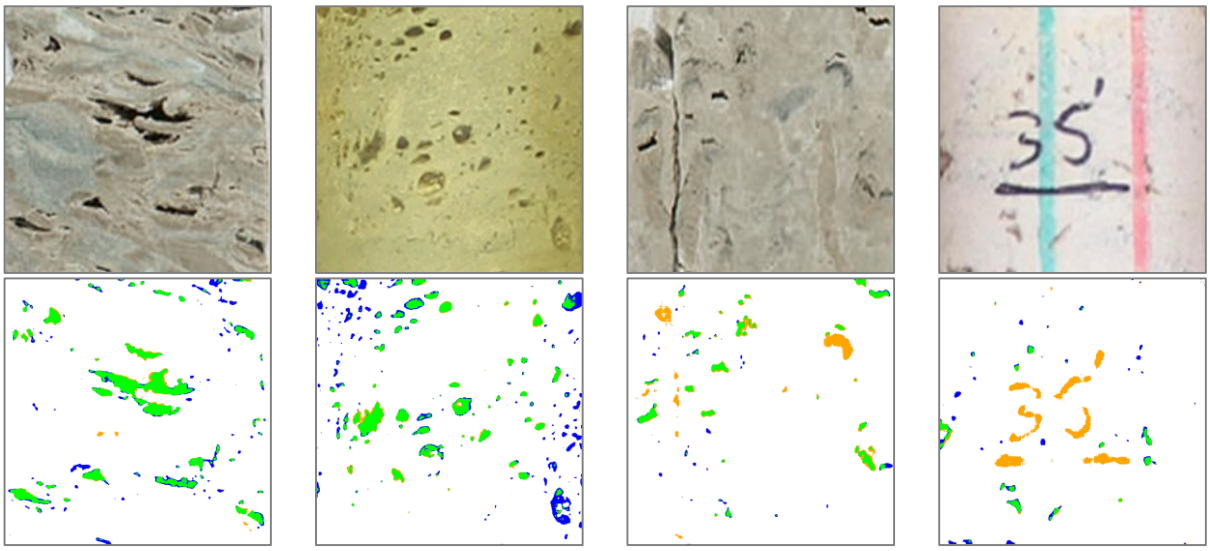


Figure 4. Examples of discrepancies between model predictions and annotations

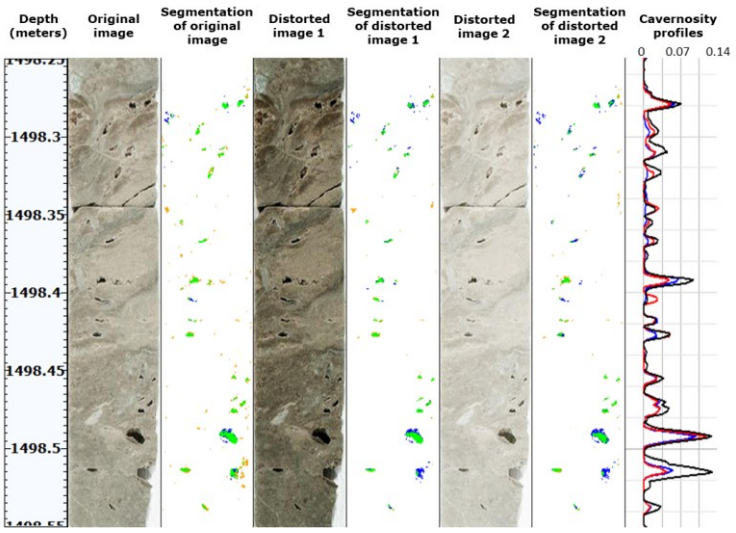



Figure 5. Segmentation results and derived profiles for a cavernous core sample

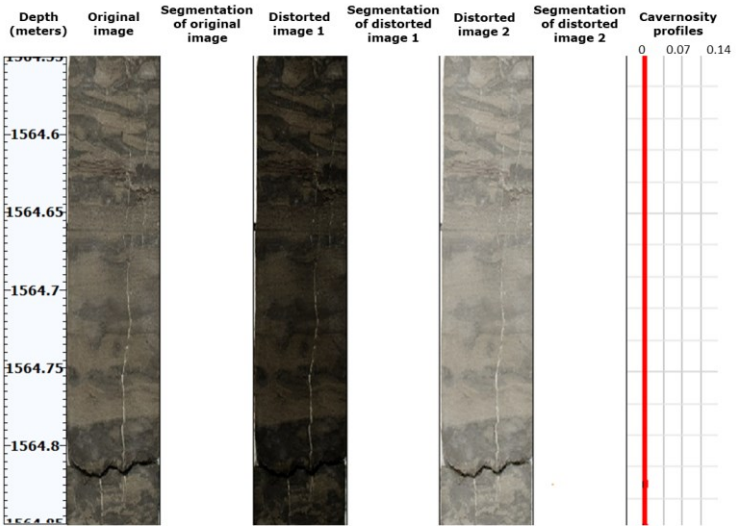



Figure 6. Segmentation results and derived profiles for a non-cavernous core sample

Figure 5 presents profiles for a core sample exhibiting visible cavernosity, whereas Figure 6 illustrates profiles for a non-cavernous core sample. Profile values, representing the fraction of pixels classified as cavern-like within a sliding window, range from 0.00 to 0.14. For pro-

files that qualitatively characterize cavernosity from core images, similarity across varying brightness distributions holds greater significance than absolute values. Figures 5 and 6 show that the profiles remain similar for the original and distorted images. Table 3 presents the pairwise Pearson correlation coefficients for the profiles in Figure 5. For the non-cavernous sample in Figure 6, the profiles remain close to zero. Thus, the proposed workflow enables the construction and visualization of cavernosity profiles from core photographs with varying brightness distributions, thereby simplifying the identification of cavernous intervals. Geological validation of the proposed profile through comparison with other geophysical data remains a subject for future work.

Table 3. Pairwise Pearson correlation coefficients for the profiles shown in Figure 5

| Profile pairs | Original, Distortion1 | Original, Distortion2 | Distortion1, Distortion2 |
|---|---|---|---|
| Correlation coefficient | 0.91 | 0.91 | 0.99 |

# Conclusion

Field development relies on geological reservoir models that require lithofacies description along well depth. Automating lithofacies delineation can improve the efficiency of geologists' work. Cavernous facies attract particular interest because they may correspond to productive intervals. Core photographs represent one of the most accessible sources of information for cavernosity analysis. These photographs enable analysis of the surface manifestation of cavernosity and support construction of a depth-dependent profile that qualitatively characterizes cavernosity. Rock heterogeneity, varying imaging conditions, fractures, and some artifacts complicate cavernosity analysis from photographs. This study proposes a deep-learning-based workflow for segmentation of cavern-like objects and construction and visualization of the cavernosity profile. The workflow includes data collection and semi-automatic cavern annotation, training of a deep learning model on augmented data, and application of the model to depth-ordered photographs for cavernosity profile construction. The method demonstrates robustness to synthetically simulated brightness variations generated by gamma correction. The results produced by the proposed workflow, including the segmentation of surface-visible caverns and the construction of a qualitative cavernosity profile, may support geologists in lithofacies description and delineation.

# References


1. Huang W., Cui Y., Xu F., Meng Z., Guo S., Zhang C. An innovative approach to permeability estimation of the fractured-vuggy carbonate reservoirs based on 2D images // Journal of Petroleum Science and Engineering, Vol. 199, 2021, 108293 (doi: 10.1016/j.petrol.2020.108293)
(https://www.sciencedirect.com/science/article/pii/S0920410520313474)

2. Gavidia J. C. R., Mohammadizadeh S., Chinelatto G. F., Basso M., Ponte Souza J. P., Portillo L. E. D., Eltom H. A., Vidal A. C., Goldstein R. H. Bridging the gap: Integrating static and dynamic data for improved permeability modeling and super k zone detection in vuggy reservoirs // Geoenergy Science and Engineering, Vol. 241, 2024, 213152 (doi: 10.1016/j.geoen.2024.213152)
(https://www.sciencedirect.com/science/article/abs/pii/S2949891024005220)

3. Li B., Tan X., Wang F., Lian P., Gao W., Li Y. Fracture and vug characterization and carbonate rock type automatic classification using X-ray CT images // Journal of Petroleum Science and Engineering, Vol. 153, 2017, pp. 88-96 (doi: 10.1016/j.petrol.2017.03.037) (https://www.sciencedirect.com/science/article/pii/S0920410517303911)

4. Cunningham K. J., Carlson J. I., Hurley N. F. New method for quantification of vuggy porosity from digital optical borehole images as applied to the karstic Pleistocene limestone of the Biscayne aquifer, southeastern Florida // Journal of Applied Geophysics, Vol. 55, № 1-

2, 2004, pp. 77-90 (doi: 10.1016/j.jappgeo.2003.06.006) (https://www.sciencedirect.com/science/article/abs/pii/S0926985103000703)
5. Li X.-N., Shen J.-S., Yang W.-Y., Li Z.-L. Automatic fracture–vug identification and extraction from electric imaging logging data based on path morphology // Petroleum Science, Vol. 16, 2019, pp. 58-76 (doi: 10.1007/s12182-018-0282-6) (https://link.springer.com/article/10.1007/s12182-018-0282-6)
6. Ausbrooks R. Quantification of vuggy porosity and lithology using borehole images, core, and logs, Bohai Basin, Offshore China. Golden, Colorado: Master's thesis, 1999.
7. Perarnau A. Use of core photo data in petrophysical analysis // SPWLA Annual Logging Symposium, Colorado Springs, Colorado, 2011, SPWLA-2011-Z (https://onepetro.org/SPWLAALS/proceedings-abstract/SPWLA11/All-SPWLA11/SPWLA-2011-Z/27939)
8. Khasanov I. I. Analiz tsvetnosti porod po tsifrovym izobrazheniyam kerna [Analysis of rock color using digital core images] // Geologiya nefti i gaza, № 5, 2014, pp. 33-39 [in Russian].
9. Altunin A. E., Semukhin M. V., Mal'shakov A. V., Yadryshnikova O. A. Sposob otsenki neftenasyshchennosti kerna gornykh porod po fotografiyam obraztsov v dnevnom svete [A method for estimating oil saturation of rock cores from daylight photographs of samples], 2018, RU 2654372 C1 [in Russian].
10. Abashkin V. V., Seleznev I. A., Chertova A. A., Istomin S. B., Romanov D. V., Samokhvalov A. F. Quantitative Analysis of Whole Core Photos for Continental Oilfield of Western Siberia // SPE Russian Petroleum Technology Conference, Society of Petroleum Engineers, 2020, SPE-202017-MS (doi: 10.2118/202017-MS) (https://onepetro.org/SPERPTC/proceedings-abstract/20RPTC/4-20RPTC/450183)
11. Seleznev I. A., Abashkin V. V., Chertova A. A., Makienko D. O., Istomin S. B., Romanov D. V., Samokhvalov A. F. Joint Usage of Whole Core Images Obtained in Different Frequency Ranges for the Tasks of Automatic Lithotype Description and Modeling of Rocks' Petrophysics Properties // Geomodel, European Association of Geoscientists & Engineers, 2020, pp. 1-5 (doi: 10.3997/2214-4609.202050090) (https://www.earthdoc.org/content/papers/10.3997/2214-4609.202050090)
12. Seleznev I. A., Makienko D. O., Abashkin V. V., Chertova A. A., Samokhvalov A. F. Variograms and Co-Occurrence Matrices in Problems of Description of Lithotypes and Modeling of Petrophysical Properties of Rocks from Whole Core Images // Geomodel, European Association of Geoscientists & Engineers, 2021, pp. 1-5 (doi: 10.3997/2214-4609.202157117) (https://www.earthdoc.org/content/papers/10.3997/2214-4609.202157117)
13. Porody gornye. Instruktsiya po otboru, konservatsii i khraneniyu kerna [Rocks. Instructions for core sampling, preservation, and storage] / STO INTI 3.180.1-2025. ANO "INTI", 2025 [in Russian].
14. Standard Practices for Preserving and Transporting Rock Core Samples / ASTM D5079-08, ASTM International, 2008.
15. Crawford B. Reviewing common core photography setups [Electronic resource]. Datarock, 2024. URL: https://datarock.com.au/reviewing-common-core-photography-setups (date accessed: 27.07.2026).
16. Potočnik M., Klemenc B., Solina F., Herlec U. Computer aided method for colour calibration and analysis of digital rock photographs // Geologija, Vol. 58, № 2, 2015, pp. 247-260 (doi: 10.5474/geologija.2015.020)
17. OpenCV. Image Thresholding [Electronic resource]. URL: https://docs.opencv.org/4.x/d7/d4d/tutorial_py_thresholding.html (date accessed: 27.07.2026).
18. Kansas Geological Survey. Kansas Core Library [Electronic resource]. University of Kansas. URL: https://www.kgs.ku.edu/Magellan/CoreLibrary (date accessed: 27.07.2026).
19. PyTorch. Torchvision [Electronic resource]. URL: https://github.com/pytorch/vision (date accessed: 27.07.2026).

20. Ronneberger O., Fischer P., Brox T. U-Net: Convolutional Networks for Biomedical Image Segmentation // Medical Image Computing and Computer-Assisted Intervention – MICCAI 2015, Lecture Notes in Computer Science, Springer, Vol. 9351, 2015, pp. 234-241 (doi: 10.1007/978-3-319-24574-4_28) (https://link.springer.com/chapter/10.1007/978-3-319-24574-4_28)

21. He K., Zhang X., Ren S., Sun J. Deep Residual Learning for Image Recognition // Proceedings of the IEEE Conference on Computer Vision and Pattern Recognition (CVPR), 2016, pp. 770-778 (doi: 10.1109/CVPR.2016.90)

22. Kingma D. P., Ba J. Adam: A Method for Stochastic Optimization // 3rd International Conference on Learning Representations (ICLR 2015), San Diego, CA, USA, 2015 (https://arxiv.org/abs/1412.6980)

23. Dagasan Y., Nguyen H., Grujic M. Inferring geological features masked by artefacts in core photography using neural networks // AEGC 2021 – Australasian Exploration Geoscience Conference, Brisbane, 2021.